Bachelor Thesis

Phase diagrams of QCD-inspired models in the large-N limit

Marc Winstel

Frankfurt am Main, 25.09.2018

Advisor & first supervisor:
Prof. Dr. Marc Wagner
Institut für theoretische Physik
Johann Wolfgang von Goethe Universität Frankfurt am Main

Second supervisor:
Prof. Dr. Dirk Rischke
Institut für theoretische Physik
Johann Wolfgang von Goethe Universität Frankfurt am Main

Abstract

In this thesis we investigate the phase diagrams of the two- and three-dimensional Gross-Neveu model in the large-N limit. A main focus is on the development of general numerical methods, which are tested by comparison with the analytically known two-dimensional model, for the investigation of phase diagrams in QCD-inspired models without making ansatzes for the chiral condensate. Then we apply them on the three-dimensional version ending up with the homogeneous diagram and first results for the inhomogeneous case.

Zusammenfassung

In dieser Thesis untersuchen wir das Phasendiagramm des zwei- und dreidimensionalen Gross-Neveu Modells im Grenzfall großer Flavorzahlen. Großer Wert liegt dabei auf der Entwicklung numerischer Methoden zur allgemeinen Untersuchung von Phasediagrammen, ohne Ansätze für den chiralen Ordnungsparametern zu wählen. Dazu wird das bereits analytisch berechnete Phasendiagramm des zweidimensionalen Gross-Neveu Models als Vergleich verwendet. Diese Methoden werden dann auf das dreidimensionale Modell angewendet, wodurch wir das homogene Phasendiagramm berechnen konnten.

Contents

1. Introduction

Quantum chromodynamics (QCD) is the theory of interaction between the fundamental components of nuclear matter, the quarks, which is realized by exchanging gauge bosons, the gluons. This so called strong interaction acts on a property called colour charge. In consequence of the non-abelian SU(3) gauge group of the theory gluons carry colour charge, which makes QCD complicated compared to quantum electrodynamics where the gauge bosons do not carry charge. For large distances and low energies the coupling is of a high scale making a perturbative access and in general analytical approaches very hard to realize. Therefore, we apply numerical computations on a discretized space-time lattice as a non-perturbative approach.

The phase diagram of QCD displays at which temperature and chemical potential the quarks exist in different phases. One central phenomenon in their distinction is confinement. It forces physical particles to be colour neutral causing the colour charged quarks to form hadrons, that are build either from quark-antiquark pairs or three quarks. At very large temperatures or chemical potential confinement is resolved and quarks exist as free excitations. This deconfined phase is also known as quark-gluon plasma.

Regarding the QCD phase diagram it is well-known that in a region of low temperature and chemical potential there exist confined quarks surrounded by a phase boundary to a deconfined phase. However, there is a region of large chemical potential and small temperature that still is subject of intense research, as another phase, called inhomogeneous phase, is suspected to be located there [Bub15]. As there exist no working approaches for computation of phase diagram for full QCD, especially in the region where the inhomogeneous phase is suspected to be located, we will investigate effective models sharing some characteristic properties with QCD. Hence, we focus on the two-dimensional and three-dimensional Gross-Neveu model in the limit of large flavor numbers(large-N limit), as it retains the chiral symmetry in common with QCD.

Phases are usually described by an order parameter that characterizes each phase with its behavior. For our model this order parameter is called the chiral condensate expressing the breaking of chiral symmetry. In the phase within the boundary this order parameter has a constant value breaking chiral symmetry, while in the phase outside the boundary it vanishes and restores the chiral symmetry. Later investigations have shown that in a region of large chemical potential and low temperature there exits a phase, where the chiral condensate has a spatial dependence, called the inhomogeneous phase. Current research investigates whether this phase also exists in more QCD-like theories.

For development of numerical techniques we will reproduce the phase diagram of the two-dimensional model because it has already analytically been solved [Th03]. Then we will expand it to three dimensions using our developed numerical tools for an investigation whether inhomogeneous phases will also occur in a two-dimensional space.

2. The Gross-Neveu model

One often used tool for research regarding the QCD phase diagram is the usage of effective models that share some symmetries with the full theory, so they are expected to reproduce some of its characteristic properties. The Gross-Neveu (GN) model, that was introduced by David Gross and Andre Neveu in 1974 [GN74], retains a discrete chiral symmetry for massless fermions while staying relatively easy to deal with. We will work on the GN model in the chiral limit and include the chemical potential via the term $\gamma_0\mu$ in the free Dirac Lagrangian. As an introduction to the properties of the GN model, we do the Lagrangian formulation and general transformations of the action in d dimensions and specify different aspects later on in the two and three dimensional case. The GN action is a sum of the free Dirac action and a four-fermion interaction term with a coupling constant g to approximate the QCD interaction. In the following we will work in an Euclidean space-time.

$$S = \int \mathrm{d}^d x \left[\sum_{j=1}^{N} \left[\bar{\psi}_j \left(\gamma^\mu \partial_\mu + \gamma_0 \mu \right) \psi_j \right] - \frac{g^2}{2} \left(\sum_{j=1}^{N} \bar{\psi}_j \psi_j \right)^2 \right] \tag{2.1}$$

Here γ^μ are the Dirac(or Gamma) matrices, which are famous from the Dirac equation and the corresponding Lagrangian, and N is our number of different flavors of fermionic fields. μ is the chemical potential. The Lagrangian of the GN model is invariant under a discrete chiral symmetry transformation

$$\psi \to \gamma_5 \psi, \ \bar{\psi} \to -\bar{\psi}\gamma_5. \tag{2.2}$$

In classical physics we could just minimize the action with respect to $\bar{\psi}$ and ψ, but in quantum theory we normally have to compute a whole path integral over all possible field configurations in the partition function, which is a difficult task when the fields occur in higher powers than quadratic. For simplification we want to get rid of the four-fermion interaction via introducing a scalar field $\sigma = -g^2 \sum_{j=1}^{N} \bar{\psi}_j \psi_j$, which represents the chiral condensate.

$$\begin{aligned} S_{\text{eff}} &= \int \mathrm{d}^d x \left(\frac{1}{2g^2}\sigma^2 + \sum_{j=1}^{N} \bar{\psi}_j \underbrace{\left(\gamma^\mu \partial_\mu + \gamma^0 \mu + \sigma \right)}_{:=Q} \psi_j \right) \\ Z &= \int \left(\prod_{i=1}^{N} \mathscr{D}\bar{\psi}_j \mathscr{D}\psi_j \right) \mathscr{D}\sigma e^{-S_{\text{eff}}} \end{aligned} \tag{2.3}$$

Now we can integrate over all fermionic field configurations applying the following formula for Grasman valued fields

$$\int \mathscr{D}\bar{\alpha}\mathscr{D}\alpha \exp\left[- \int \mathrm{d}^{\mathrm{d}} x \ \mathrm{d}^{\mathrm{d}} y \ \bar{\alpha}(x) M(x,y) \alpha(y) \right] = \det(M). \tag{2.4}$$

Raising the determinant back into the exponent we get with the definition $\lambda \coloneqq N * g^2$

$$S_{\text{eff}} = N\left(\frac{1}{2\lambda}\int \mathrm{d}^d x\sigma^2 - \ln\left(\det(Q)\right)\right)$$
$$Z = \int \mathscr{D}\sigma e^{-S_{\text{eff}}}. \tag{2.5}$$

To be able to apply (2.4) in the context of (2.3), we need $\det(Q)$ to be real and positive, which is checked for the $1+1$-dimensional and the $1+2$-dimensional GN model in the following section. With this simplifications we apply our large-N limit $N \to \infty$ suppressing any contribution besides the minimum of the effective action. So basically, we have to search for the chiral condensate that minimizes the effective action like in the classical case to get the physical configuration of σ due to the large-N limit. Notice that we explicitly search for inhomogeneous phases, so this configuration should be allowed to be spatially dependent $\sigma = \sigma(\vec{x})$.

The chiral symmetry is now expressed via the chiral condensate σ, that acts like a typical mass term in quantum field theory. Due to the definition of σ the chiral symmetry transformation for 2.5 is

$$\sigma \to -\sigma. \tag{2.6}$$

Hence, the Lagrangian retains its chiral symmetry for vanishing chiral condensate. If we find a finite value of σ via minimization at a certain phase point, this symmetry will be broken dynamically.

2.1. Gross-Neveu in 1+1 dimensions

As said before, it is essential to ensure that the determinant of the Dirac operator is real and positive to get our effective action as in (2.5). In $1+1$ dimensions there is a simple proof for $\det(Q) \in \mathbb{R}$ without specifying our choice of Dirac matrices. We will look at the eigenvalue equation for Q, since the determinant of an operator is the product of its eigenvalues. The eigenvalue equation of the Dirac operator of the $1+1$ dimensional GN-model with the eigenfunction f is

$$Q \cdot f = (\gamma^\mu \partial_\mu + \gamma^0 * \mu + \sigma) \cdot f = \lambda f. \tag{2.7}$$

For our proof we will complex conjugate (2.7).

$$[(\gamma^0)^*\partial_0 + (\gamma^0)^*\mu + (\gamma^1)^*\partial_1 + \sigma] \cdot f^* = \lambda^* f^* \tag{2.8}$$

The gamma matrices have to fulfill Clifford algebra

$$\{\gamma^\mu, \gamma^\nu\} = 2g^{\mu\nu}\mathbb{1}_2 \tag{2.9}$$

with $\mathbb{1}_2$ being the identity in two dimensions, because the spinor space can be reduced to two components in the two dimensional case. Since the Euclidean and Minkowski signature are real and diagonal, also γ_μ^* (as well as γ_μ^T and $\gamma_\mu^\dagger$) generate the Clifford algebra. [Park05, page 3] points out that this implies that γ_μ^* are related to γ_μ by an unitary similarity transformation in even dimensions, which is unique up to some constant and preserves the eigenvalues. We define this transformation with

$$(\gamma^\mu)^* = B \cdot \gamma^\mu \cdot B^{-1}. \tag{2.10}$$

One can insert this relation into (2.8)

$$(B \cdot \gamma^0 \cdot B^{-1}\partial_0 + B \cdot \gamma^0 * B^{-1} \cdot \mu + B \cdot \gamma^1 \cdot B^{-1}\partial_1 + \sigma \cdot BB^{-1}) \cdot f^* = \lambda^* f^* \tag{2.11}$$

Now we can multiply with B^{-1} from the left to get the Dirac operator Q back on the left side.

$$Q \cdot B^{-1} \cdot f^* = (\gamma^0\partial_0 + \gamma^0\mu + \gamma^1\partial_1 + \sigma) \cdot B^{-1} \cdot f^* = \lambda^* \cdot B^{-1} \cdot f^* \tag{2.12}$$

Concluding, this means λ^* is eigenvalue to the eigenfunction $B^{-1} * f^*$, if (2.7) is fulfilled. Now we have to examine two different cases. In case of $\Im(\lambda) \neq 0$ for all λ it is ensured now that $\det(Q) \geq 0$ and $\det(Q) \in \mathbb{R}$ as it is a product of a complex conjugated pair of eigenvalues. If λ is real, we have also ensured that $\det(Q)$ is real, but we cannot secure that $B^{-1} * f^* \neq f$, so it is possible that there exists another real, possibly negative eigenvalue of the Dirac operator. This means we cannot proof the positivity of $\det(Q)$. However, we never obtained a negative determinant in our numerical computation.

2.1.1. Choice of representation

Since we have not specified our Dirac matrices in the beginning, we will do that in the following. In 2 dimension we can simply use the from quantum mechanics well-known Pauli matrices as they fulfill the Clifford algebra in Euclidean space-time ($g_{\mu\nu} = \delta_{\mu\nu}$).

$$\{\sigma_i, \sigma_j\} = 2\delta_{ij}\mathbb{1}_2 \tag{2.13}$$

As we only need two matrices, we choose $\gamma_0 = \sigma_1$ and $\gamma_1 = \sigma_3$. With this set of Dirac matrices we can represent $\det(Q)$ as a simple sum over its eigenvalues, that can be computed directly, for constant value of chiral condensate via solving the eigenvalue equation. This is done extensively for three dimensions in 2.2.2, but works analogous in two dimensions.

2.2. Gross-Neveu in 1+2 dimensions

For the three-dimensional GN theory the same proof for $\det(Q) \in \mathbb{R}$ as in two dimensions does not work when applying an irreducible representation. Searching for an explanation we take a look at the construction of matrices that fulfill the Clifford algebra in odd dimensional theories.

With d being a odd number the irreducible representation in d dimensions is build via combining the Dirac matrices of the $(d-1)$-dimensional irreducible representation with the chirality operator that is famous as γ^5 in four dimensions. We use the following definition of the chirality operator in $(d-1)$ dimensions with an Euclidean signature to generate a linear independent third matrix

$$\gamma^{\text{chiral}} := i^{\frac{d-1}{2}} \prod_{\nu=0}^{d-1} \gamma^{\nu}. \tag{2.14}$$

The problem with this set of Dirac matrices,where $\gamma_2 := \gamma_{\text{chiral}}$, is that we are not able to apply the same argumentation used in 2.1 because we can not simply reproduce the Dirac operator out of its complex conjugated via inserting the similarity transformation (2.10) as we get an additional factor i that we also have to complex conjugate. This has a more mathematical background. The behavior of the additional Dirac matrix under transformations is studied in [Park05, page 6 and following]. To guarantee the realness of $\det(Q)$ in the same way as in 2.1 one could go into a reducible representation, where it would work perfectly using the usual representations from four dimensional theories. This is however unfavorable due to other problems occurring, that are mentioned in the next section. But although this general procedure fails for the irreducible case, we obtain nevertheless a real $\det(Q)$ in our numerical computation, which forces us to search for other arguments to justify our result.

2.2.1. Reducible representation

For a first investigation we will restrict to spatially constant value of the chiral condensate, choose an explicit set of Dirac matrices and calculate the eigenvalues explicitly, which will give us a real result. Being uncertain whether the irreducible representation also leads to a real determinant for inhomogeneous chiral condensate we also explored reducible representations. Even though we are able to use an irreducible one in our computation, we will show the connection and differences between both representations, since we can for sure guarantee the determinant in reducible representation, $\det(Q_4)$, being real. Therefore, let us have a closer look to the definition of irreducibility.

Definition: A representation of a group in a $\mathbb{K}$-vector space V is irreducible, if $V \neq 0$ and V and 0 are the only subspaces, which are invariant under the group.

For our matrix representation this means, if our Dirac matrices contain smaller subspaces that also fulfill the Clifford algebra (2.9), we have a reducible representation that

could be broken down to an irreducible one. Obviously most times one is interested in the irreducible representation because a reducible (4×4) representation doubles the spinor space and simultaneously creates two different amounts of flavors, which transform differently under the Dirac matrices and maybe could produce different physics than our original system, out of one infinite amount. Nevertheless we want to create a reducible one for our model, because we are interested in the connection between both representations. We can construct a set of 4×4 Dirac matrices out of tensor products with our two dimensional representations 2.1.1 using the Pauli matrices again. The exact procedure is given in [Gm18], but we have to be careful as we have to adapt it when using the Euclidean signature. We end up with

$$\gamma^0 = \begin{pmatrix} \sigma^1 & 0 \\ 0 & \sigma^1 \end{pmatrix} \; \gamma^1 = \begin{pmatrix} \sigma^3 & 0 \\ 0 & -\sigma^3 \end{pmatrix} \; \gamma^2 = \begin{pmatrix} \sigma^2 & 0 \\ 0 & \sigma^2 \end{pmatrix} \; \gamma^3 = \begin{pmatrix} 0 & \sigma^3 \\ \sigma^3 & 0 \end{pmatrix}. \tag{2.15}$$

Now we have constructed a set of 4 Dirac matrices. In the following we will only choose γ_0, γ_1 and γ_2, that we use as a reducible representation for the $1+2$-dimensional GN model. These three matrices contain the three Pauli matrices in a block diagonal way. This fact we can use for an investigation of the connection between $\det(Q_4)$ and the determinant in the irreducible representation, $\det(Q_2)$.

2.2.2. Computation of Dirac determinant

For computation of the determinant, we solve the eigenvalue equation of the Dirac operator (2.7) for translationally invariant σ. We make a plane wave ansatz for the eigenfunction, as they are eigenfunction of a continuum derivative as well as of a lattice derivative.

$$\begin{pmatrix} f_1 \\ f_2 \end{pmatrix} = \begin{pmatrix} v_1 \\ v_2 \end{pmatrix} e^{i(k_0 x_0 + k_1 x_1 + k_2 x_2)} \tag{2.16}$$

v_1, v_2 are constants and $x_i \, (i = 0, 1, 2)$ are the three directions in space-time, where x_0 denotes the time coordinate. k_i denotes the corresponding momentum.
Applying periodic boundary conditions in the two spatial directions and anti-periodic boundary condition in time direction quantizes the momenta.

$$\begin{aligned} &k_0 = \frac{2\pi\left(n_t - \frac{1}{2}\right)}{T}; \qquad k_1 = \frac{2\pi n_x}{L}; \qquad k_2 = \frac{2\pi n_y}{L} \\ &n_t = -N_t + 1, \ldots, N_t - 1, N_t; \quad n_x = 0, 1, 2, \ldots, L-1; \quad n_y = 0, 1, 2, \ldots, L-1 \end{aligned} \tag{2.17}$$

Here L is the spatial extent of our system and $T = 2N_t$ is the temporal extent, taking into account that we have even and odd modes. We do the calculation with continuum derivatives for simplicity, but it works analogous for lattices derivatives with the replacement $k_i \to sin\,(k_i)$.

With this ansatz we can compute the eigenvalues of Q_2 in dependence on our momenta via the characteristic polynomial

$$\det \begin{pmatrix} ik_1 + \sigma - \lambda & ik_0 + \mu + k_2 \\ ik_0 + \mu - k_2 & -ik_1 + \sigma - \lambda \end{pmatrix} \stackrel{!}{=} 0. \tag{2.18}$$

Solving this quadratic equation in lambda delivers two eigenvalues, which corresponds to the fact that we wrote out the matrix in spinor space, but not in momentum space.

$$\lambda_{1/2} = \sigma \pm i\sqrt{k_0^2 + k_1^2 + k_2^2 - \mu^2 - i2\mu k_0} \tag{2.19}$$

As $\lambda_{1/2}$ depend on our momenta, we get

$$\begin{aligned}
\det(Q_2) &= \prod_{k_0,k_1,k_2} \lambda_1\lambda_2 = \prod_{k_0,k_1,k_2} \left[\sigma^2 - \mu^2 + k_0^2 + k_1^2 + k_2^2 - 2i\mu k_0\right] \\
&= \prod_{n_t=-N_t+1}^{N_t} \prod_{n_x=0}^{L-1} \prod_{n_y=0}^{L-1} \left[\sigma^2 - \mu^2 + \left(\frac{2\pi n_x}{L}\right)^2 + \left(\frac{2\pi n_y}{L}\right)^2 + \left(\frac{(2n_t-1)\pi}{T}\right)^2 - 2i\mu\frac{(2n_t-1)\pi}{T}\right] \\
&= \prod_{n_t=1}^{N_t} \prod_{n_x=0}^{L-1} \prod_{n_y=0}^{L-1} \left[\left\{\sigma^2 - \mu^2 + \left(\frac{2\pi n_x}{L}\right)^2 + \left(\frac{2\pi n_y}{L}\right)^2 + \left(\frac{(2n_t-1)\pi}{T}\right)^2\right\}^2 + \left\{2\mu\frac{(2n_t-1)\pi}{T}\right\}^2\right].
\end{aligned} \tag{2.20}$$

In the last step we shifted the product over n_t and made use of the multiplication of complex paired eigenvalues. As $\det(Q_2)$ is now expressed as a product of squares of absolute values taken from its eigenvalues, it must be real and positive due to the properties of the absolute value. By the way, for $1+1$-dimensional space-time this computation works the same yielding an analogous result with omitting one term containing the eigenvalue of one spatial dimension in (2.20).

Using block diagonal representation (2.15), we can additionally show a simple relation between $\det(Q_4)$ and $\det(Q_2)$ for homogeneous σ.

$$Q_4 = \begin{pmatrix} \sigma + \partial_1 & \partial_0 + \mu - i\partial_2 & 0 & 0 \\ \partial_0 + \mu + i\partial_2 & \sigma - \partial_1 & 0 & 0 \\ 0 & 0 & \sigma - \partial_1 & \partial_0 + \mu - i\partial_2 \\ 0 & 0 & \partial_0 + \mu + i\partial_2 & \sigma + \partial_1 \end{pmatrix} \tag{2.21}$$

The starting point is again (2.7) for Q_4. As the matrix is in a blockdiagonal form, we can make two ansatzes for the eigenfunction.

$$f_1 = \begin{pmatrix} v_1 \\ v_2 \\ 0 \\ 0 \end{pmatrix} e^{i(k_0x_0+k_1x_1+k_2x_2)} \qquad f_2 = \begin{pmatrix} 0 \\ 0 \\ u_1 \\ u_2 \end{pmatrix} e^{i(k_0x_0+k_1x_1+k_2x_2)} \tag{2.22}$$

$$v_i, u_i = const. \text{ with } i = 1, 2$$

The determinant factorizes into the determinants of the both 2×2 blocks that Q_4 contains. Applying (2.22) we can replace each derivative with the corresponding momentum.

$$\det(Q_4) = \det\begin{pmatrix} ik_1 + \sigma & ik_0 + \mu + k_2 \\ ik_0 + \mu - k_2 & -ik_1 + \sigma \end{pmatrix} \det\begin{pmatrix} -ik_1 + \sigma & ik_0 + \mu + k_2 \\ ik_0 + \mu - k_2 & ik_1 + \sigma \end{pmatrix} \tag{2.23}$$

Because all components are numbers now, we can conclude due to Sarrus' rule

$$\begin{aligned}&\det(Q_4) = \det(Q_2)^2\\ &= \prod_{n_t=1}^{N_t}\prod_{n_x=0}^{L-1}\prod_{n_y=0}^{L-1}\left[\left\{\sigma^2-\mu^2+\left(\frac{2\pi n_x}{L}\right)^2+\left(\frac{2\pi n_y}{L}\right)^2+\left(\frac{(2n_t-1)\pi}{T}\right)^2\right\}^2+\left\{2\mu\frac{(2n_t-1)\pi}{T}\right\}^2\right]^2.\end{aligned} \tag{2.24}$$

This connection between the reducible representation (2.15) and the irreducible one(2.1.1) for the translationally invariant condensate supports our numerical findings of $\det(Q_2)$ being real, as the choice of a reducible representation yields a real determinant even in case of a spatial dependent condensate.

The following method to show the realness of $\det(Q_2)$ works also in the spatially dependent case and leads to breaking it down to the symmetry $\det(Q_2(\sigma)) = \det(Q_2(-\sigma))$. Thus, we look again at the complex conjugated eigenvalue equation (2.7) for Q in representation of the Pauli matrices (2.1.1), where only one of the Dirac matrices is complex valued.

$$(\sigma_1(\partial_0+\mu)-\sigma_2\partial_1+\sigma_3\partial_2+\sigma)\cdot f^* = \lambda^* f^* \tag{2.25}$$

Multiply with σ_2 from the left and from the right and applying the properties of the Pauli matrices leads to

$$(\sigma_1(\partial_0+\mu)+\sigma_2\partial_1+\sigma_3\partial_2-\sigma)\cdot f^* = -\lambda^* f^* \tag{2.26}$$

From this equation we can conclude the relation

$$\lambda \text{ is eigenvalue to } Q_2(\sigma) \leftrightarrow (-\lambda^*) \text{ is eigenvalue to } Q_2(-\sigma).$$

With this equivalence and the assumption that Q_2 has an even dimension we get

$$\det\left(Q_2\left(\sigma\right)\right)^* = \prod_i \lambda_i^* = \prod_i(-\lambda_i^*) = \det\left(Q_2\left(-\sigma\right)\right). \tag{2.27}$$

Basically we have broken the condition for realness $\det(Q_2)^* = \det(Q_2)$ down to the demand of $\det(Q_2)$ being an even function in σ. For a full analytical proof for $\det(Q_2) \in \mathbb{R}$ we still have to show

$$\det(Q_2(-\sigma)) \stackrel{!}{=} \det(Q_2(\sigma)) \tag{2.28}$$

which we have not been able to proof yet. As a numerical test we have computed $\det(Q_2(\sigma))$ and $\det(Q_2(-\sigma))$ for constant and spatially dependent condensate, which has been generated via a random number algorithm, and different lattice sizes using a LU-decomposition for calculation and received the same results within the precision of double variables used in C programming. Also we computed the phase of $\det(Q_2(\sigma))$ and got a phase factor of zero for every setup tested.
To conclude, we have done several investigations trying to guarantee a real and positive $\det(Q)$, which we were not able to fully proof in a analytical way. Nevertheless, we have gotten many analytical arguments and hints that help to justify our numerical results. Therefore, we use the effective action (2.5) for computation of the phase diagram.

3. Implementation and numerical methods

The GNU scientific library (GSL) is used in our code for several numerical functionalities. The code base for the two-dimensional model has been provided by Marc Wagner. Calculations on the FUCHS-CSC high-performance computers of Goethe University Frankfurt have been conducted for this research. We would like to thank HPC-Hessen, funded by the State Ministry of Higher Education, Research and the Arts, for programming advice.

In our setup we have periodic boundary conditions in space with spatial lattice extent L and an anti-periodic boundary in time direction with temporal extent T and the corresponding temperature $\theta = \frac{1}{T}$. We use a hybrid of a plane wave discretization for the time direction and a naive lattice discretization in space, that obviously causes fermion doubling as a pure lattice artifact (in detail explained in [GL10]), but this should not bother us as we already work in the large-N limit. The basis functions for the plane waves are $\sin(k_{n_t} t)$ and $\cos(k_{n_t} t)$ with $k_{n_t} = \frac{(2n_t - 1)\pi}{T}, \quad n_t = 1, 2, \ldots, N_t$.

We want to apply a density for the degrees of freedom (dofs) $\rho = \frac{\text{number of dofs}}{\text{lattice size}} = 1$ in the spatial direction. To have the same density in temporal direction, we choose a momentum cutoff $w_{cut} = \pi$, implying the relation $T = 2N_t$. As the inverse temporal extent corresponds to the temperature we have to take more and more modes in account for computation when wanting to calculate lower temperatures. The coupling constant λ is set after calculating the temperature θ_c for $\mu = 0$ and a fixed parameter $N_{t,c}$ and varying the coupling until the phase boundary, determined with the second derivative in sigma of the action as presented in 3.1, occurs at θ_c. With setting λ for this given parameters, we ensure a scaling for our temperature computation via modes about the assignment of $N_{t,c}$ to θ_c. This parameter $N_{t,c}$ that must be set in the code gives the number of modes, that are used in the computation for this critical temperature, and therefore, gives the precision of whole temperature computation within the phase diagram. The lattice spacing a_t is then given by θ_c divided by the temporal lattice extent. Later (4) we will investigate at which choice of parameters facilitate an accurate calculation is possible. Also it is important to have a spatial volume larger than in time direction, because in the search for inhomogeneous phase we could get incommensurability effects with the spatially dependent condensate for too small spatial volumes [dFW06, Figure 1]. These incommensurability effects occur besides the standard finite volume effect caused by the finite extent of our lattice.

As usual in lattice computation we work in dimensionless units. Thus, at the start of a computation we go to a small temperature at $\mu = 0$, corresponding to a large cutoff number for modes $N_{t,0}$, minimize the effective action and get the value of the chiral condensate σ_0. In the phase diagram we will work in units of this σ_0.

3.1. Determination of homogeneous boundary

For a first investigation we want to produce a homogeneous phase diagram, therefore we only allow spatially constant values for the chiral condensate. In this case we can compute the determinant of the Dirac operator via solving the eigenvalue equation with lattice discretization in spatial direction and a plane wave expansion in time direction as it has already been presented for the three-dimensional case in 2.2.2. So we can simply compute the effective action (2.5) by implementing this analytical solution. The chiral condensate has the value σ, that minimizes the effective action for given μ and θ. For the phase diagram we will decide between first order boundary, where a discontinuity in the order parameter occurs, and second order phase boundary, where the order parameter goes continuously against zero. This difference can be visualized by a investigation of the effective action near the phase boundary. Thus, we plot the effective action of the $1+1$-dimensional GN model against the value of the chiral condensate for parameters corresponding to both phases 3.1. In the chirally broken phase the effective action looks like a Mexican hat function, this means the minimum is located clearly at a finite value of σ while S_{eff} $(\sigma = 0)$ is a maximum. However, in the restored phase we have a parabola-like behavior with a minimum at vanishing σ. The distinction between the both orders

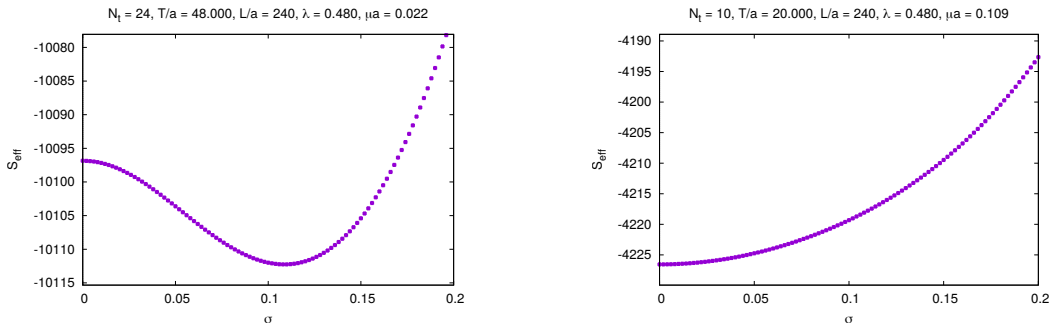

(a) Chirally broken phase

(b) Chirally restored phase

Figure 3.1: Effective actions of $1+1$-dimensional GN model in each phase

of boundaries is obtained by plotting the action nearby the left side of the boundary, because we have to expect different behavior of the effective action for first and second order. This follows from the physical value of σ being computed via minimization of S_{eff}. At the first order boundary in the Mexican hat form a maximum emerges (fig 3.2(a)). The maximum gets closer to the minimum when raising the chemical potential from the chirally broken phase to the restored phase until the functional behavior changes to a parabola, which is when σ suddenly changes from a finite value to zero at the boundary. At second order boundary we obtain a continuous deforming of the Mexican hat (fig 3.1(a)), when raising chemical potential, so that the minima moves continuously against zero guaranteeing the continuity of the condensate at the boundary.

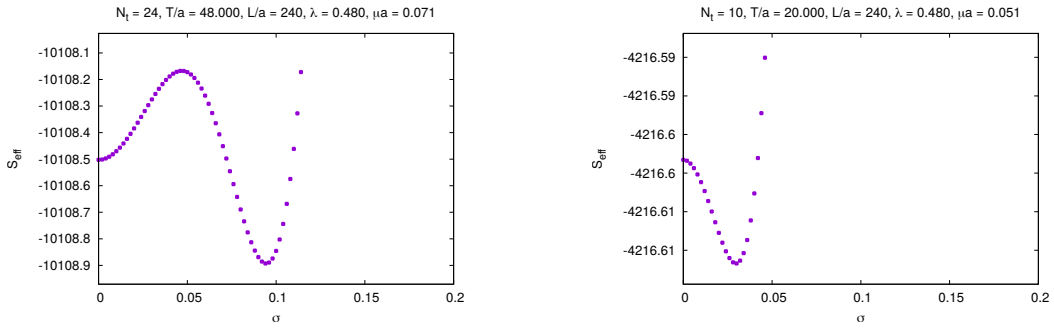

(a) First order

(b) Second order

Figure 3.2: Effective actions of $1+1$-dimensional GN near phase boundary

Given this analysis of effective action for both boundaries we can implement methods to identify whether a first or a second order boundary occurs. The determination of the phase boundary always starts at a given temperature, so we have to search for the chemical potential at which the phase boundary is located. The second order phase boundary can be determined via calculating the second derivative with respect to sigma of the effective action at $\sigma = 0$. At the phase boundary $\frac{\partial^2}{\partial\sigma^2} S_{\text{eff}}\big|_{\sigma=0}$ will change sign, as zero is the minimum of S_{eff} in the chirally restored phase, but a maximum in the chirally broken phase, so we can determine the phase boundary via a bisection where we calculate $\frac{\partial^2}{\partial\sigma^2} S_{\text{eff}}\big|_{\sigma=0}$ iterative. The calculation of the second derivative has been done analytically, because we already computed S_{eff} like in 2.2.2, due to better precision of the result. If we have found a second order phase boundary at μ_b, we will check for first order boundary. Therefore we use a minimization algorithm for S_{eff} of GSL to find the physical value of σ for a tuple (μ, T). As a condition for first order boundary we can now determine whether $\sigma(\mu_b - \epsilon) \neq 0$ and $\sigma(\mu_b + \epsilon) = 0$, with properly chosen ϵ. For a solid proposition of the choice of ϵ more research is needed.

3.2. Instability analysis for inhomogeneous boundary

Computing the inhomogeneous phase boundary takes a lot more effort than for the homogeneous, as we allow spatially dependent $\sigma(\vec{x})$. To produce the exact inhomogeneous phase boundary, we have to treat the chiral condensate as a spatially dependent function. Putting it on the lattice, the infinite amount of degrees of freedom is reduced to a finite number of independent variables σ_i, where $i = 0, 1, \ldots, L^d - 1$, when d is the number of spatial dimensions. Consequently, the effective action on the lattice is a function working on the space of independent variables σ_i. For the correct phase boundaries we would therefore need a minimization in these σ_i. This minimization in several variables is a huge numerical (and analytical) task that is addressed in the mathematical field of optimization and has not been applied yet.

In following studies an implementation of such an minimization algorithm will be required. Instead we do an instability analysis for $\sigma_i = 0 \quad \forall i$ to determine the boundary between chirally restored and inhomogeneous phase. Due to the requirement on huge computation power of this analysis, most inhomogeneous results presented have been conducted on FUCHS-CSC high performance computers.

As a first step for the analysis we need to be able to compute the second derivative of the effective action, which leads to the second derivative of $\ln(\det(Q))$ in σ. For $\ln(\det(Q))$ we compute each matrix element of Q numerically and then use GSL for a LU-decomposition, that is useful for calculating $\ln(\det(Q))$ directly via the libraries functions. The Dirac operator is in this computation represented by a product of matrices, as we factorize out the number of modes N_t, since our condensate is not time dependent. We need the Hessian matrix H_{ij} with matrix elements $\frac{\partial^2}{\partial_{\sigma_i}\partial_{\sigma_j}} S_{\text{eff}}$ to investigate instability of the vanishing chiral condensate. A derivative $\frac{\partial}{\partial_{\sigma_i}}$ working on $\ln(\det(Q))$ can be calculated via the method of finite differences, where we vary the value of σ at the lattice point i in positive and negative direction and calculate the differential quotient in $\ln(\det(Q))$.

As this computation is very expensive in runtime due to the several calls of the $\ln(\det(Q))$-function, we want to exploit symmetries in the Hessian to save some time. For a detailed discussion of computation time and exploitation of symmetries for $1+1$- and $1+2$-dimensional GN model see 3.3.2. Now we are able to calculate the Hessian matrix, so we can do an instability analysis via calculation the eigenvalues of H_{ij} for $\sigma_i = 0 \quad \forall i$. This is also done with the functionalities of GSL. If we find one negative eigenvalue in this procedure, this means $\sigma = 0$ is not a stable minimum and we are able to find a direction in the space of σ_i, of which the effective action is a function that leads to a lower effective action. The form of this vector can be read of the eigenvectors that correspond to the negative eigenvalue. Keeping this in mind, we are able to find the phase boundary between the chirally restored phase and the inhomogeneous phase. For two dimensions it is a little bit easier to evaluate the result of this method as we are aware of the analytical solution 4.1. As for small chemical potential we find the chirally broken phase, we can find the value of μ where $\sigma = 0$ starts to be a stable minimum giving us the phase boundary between the spatially dependent and the chirally restored phase via bisection for given temperature. We are not able to find the other phase boundary from the chirally broken to the inhomogeneous phase, since the instability analysis can only be done for vanishing chiral condensate, which is not a stable solution in both phases. This recquires the development of better techniques. Nevertheless, as we are able to compute the homogeneous phase diagram, we can at least compute one arm of the phase boundary and estimate the region of the inhomogeneous phase.

3.3. Runtime analysis

3.3.1. Discussion of computation time

As we want to receive accurate results arose from large enough lattice parameters while avoiding huge runtimes, we explore the computation time behavior. We have to difference between the homogeneous and inhomogeneous phase diagram, since they work with totally different methods. The homogeneous calculations work basically with arithmetic operations iterated with loops, whose length depend on our parameters N_t and L as the eigenvalues of the Dirac operator depend on spatial and temporal momenta. In consequence, computation time depends linear on spatial extent and mode number N_t in two dimensions and in the three-dimensional case linear on the mode number and quadratic on the lattice extent. Obviously, we need to compute the same number of points to compare the computation time directly, but it can also be interesting to see differences when going further to large mode numbers corresponding to low temperatures. $N_{t,\max}$ is the maximum number of modes, for which a boundary is calculated.

We see from the data in table 1 that the calculation of large mode cutoff takes not much more time than for small mode cutoff, for example halving the number of modes for critical temperature. But for set critical mode number it takes significantly more time to calculate the half of points, that corresponds to a lower temperature. The expected, linear dependence on the spatial extent for the $1+1$-dimensional model is nearly fulfilled.

$N_{t,c}$	$N_{t,\max}$	Spatial extent$L$	Computation time [sec]
8	24	240	$3.11 \cdot 10^0$
8	48	120	$8.04 \cdot 10^0$
8	48	240	$1.69 \cdot 10^1$
8	48	480	$3.25 \cdot 10^1$
16	56	240	$1.70 \cdot 10^1$

Table 1: Computation time for homogeneous phase diagram for $1+1$-dimensional GN model

From table 2 we obtain the quadratic dependence on the spatial extent of our lattice in good approximation. Also the calculation including larger mode numbers increases considerably compared to smaller mode number at fixed critical mode number $N_{t,c}$. We save a small amount of time, when calculating the same amount of boundaries with a smaller critical mode number, but the computation time saved is minor to the possible loss in precision of our computation.
For the inhomogeneous case, we conducted some calculations on FUCHS-CSC high performance computers and others on regular desktop computers. For the work on FUCHS-CSC we parallelize our code in computing single phase points and run tasks parallel on different CPU cores to produce a phase diagram. To make a comparison between both methods possible, we compare computation time of single phase points.

$N_{t,c}$	$N_{t,\max}$	Spatial extent$L$	Computation time [sec]
10	60	60	$8.36 \cdot 10^2$
10	60	360	$2.98 \cdot 10^4$
10	30	60	$1.83 \cdot 10^2$
4	24	60	$1.61 \cdot 10^2$
4	24	120	$6.30 \cdot 10^2$

Table 2: Computation time for homogeneous phase diagram for $1+2$-dimensional GN model

For more detailed runtime analysis for the computation of the Hessian matrix look at the following section. Of course, we use in every computation the same accuracy for the bisection determining the boundary.

$N_{t,c}$	N_t	Spatial extent$L$	Computation time [sec]
4	16	80	$7.60 \cdot 10^2$
8	20	80	$9.05 \cdot 10^2$
8	20	160	$2.32 \cdot 10^4$
8	20	240	$1.24 \cdot 10^5$
8	40	160	$4.57 \cdot 10^4$
8	40	240	$2.48 \cdot 10^5$

Table 3: Computation time of one phase point for $1+1$-dimensional GN model

We see a linear dependence in the mode number N_t in both tables 3 and 4, that could be expected as the determinant factorizes into a product, where each factor corresponds to one mode. The values show an order of dependence on the lattice extent between $\mathcal{O}\left(L^4\right)$ and $\mathcal{O}\left(L^5\right)$ in the data of the two-dimensional model. For table 4 we could guess an approximate dependence of $\mathcal{O}\left(L^8\right)$. This would sufficiently fit our expectation described in detail for the computation of a single Hessian matrix in 3.3.2. Because the data shows no clear order of dependence, a more solid investigation is needed.

$N_{t,c}$	N_t	Spatial extent$L$	Computation time [sec]
4	12	6	$9.93 \cdot 10^1$
4	12	8	$8.02 \cdot 10^2$
4	6	10	$6.64 \cdot 10^2$
4	6	16	$1.55 \cdot 10^5$
4	12	16	$3.10 \cdot 10^5$
4	6	20	$8.66 \cdot 10^5$

Table 4: Computation time of one phase point for $1+2$-dimensional GN model

3.3.2. Application of symmetries to the Hessian matrix

The computation of the Hessian matrix, that is iterated several times in our code for the calculation of the phase diagram, takes a large amount of computation time. Compared to this huge computational effort the calculation of eigenvectors and eigenvalues is quite fast. Therefore, saving as much runtime as possible via exploiting all symmetries of our system is required. For every entry in the Hessian matrix we have to calculate the second derivative of $\ln(\det(Q))$ via finite difference. The calculation of $\ln(\det(Q))$ works with a LU-decomposition, which has a computation time behavior of third order of matrix size. For the two-dimensional case this means $\mathcal{O}\left(L^3\right)$, for three dimensions $\mathcal{O}\left(L^6\right)$. Now we will explore the dependence on lattice size of the amount of calls of the function, that calculates the second derivative of $\ln(\det(Q)))$. For one spatial dimension the exploited symmetries are parity and the translation invariance of the Hessian matrix. So we have to only really compute half of the first row of the Hessian and match the rest of its entries with the computed values. This reduces the dependence of call time on the lattice size from $\mathcal{O}\left(L^2\right)$ to $\mathcal{O}\left(L\right)$. In two spatial dimensions we are also able to apply the translational and parity invariance for both spatial directions. Additionally we can use the isotropy of the system that halves our runtime. Here we find a reduction from $\mathcal{O}\left(L^4\right)$ to $\mathcal{O}\left(L^2\right)$ for the call time of the $\ln(\det(Q))$-function.
Concluding, the whole runtime for the Hessian has a dependence of $\mathcal{O}\left(L^5\right)$ reduced to $\mathcal{O}\left(L^4\right)$ via symmetries in the two-dimensional model and of $\mathcal{O}\left(L^{10}\right)$ reduced to $\mathcal{O}\left(L^8\right)$ for three dimensions. In three dimensions, this leads to huge computation times for lattice sizes, that could produce a phase transition nearby the continuum case. Hence, we have to accept significant finite volume effects according to the current situation. For illustration we compare the runtime of one Hessian matrix in both models at the same phase point for various lattice sizes without and with making use of symmetries. The

Dimension	Lattice size	Computation time without exploiting symmetry [sec]	Computation time with exploited symmetry [sec]
$1+1$	40	$1.07 \cdot 10^2$	$1.42 \cdot 10^0$
$1+1$	60	$6.62 \cdot 10^2$	$5.61 \cdot 10^0$
$1+1$	80	$2.50 \cdot 10^3$	$1.58 \cdot 10^1$
$1+2$	4	$1.93 \cdot 10^1$	$3.26 \cdot 10^{-1}$
$1+2$	6	$6.69 \cdot 10^2$	$4.48 \cdot 10^0$
$1+2$	8	$9.59 \cdot 10^3$	$3.57 \cdot 10^1$
$1+2$	16		$4.68 \cdot 10^3$

Table 5: Comparison of computation time for Hessian matrix for both GN-models $N_{t,c} = 4$, $\mu = 0.2\sigma_0$, $\theta = \frac{1}{12*\sigma_0}$

data in table 5 shows the theoretically expected behavior within some deviation in the three-dimensional case, that results from the small test parameters causing lower orders of L to also make a significant contribution. These list of our first measurements shows that the computation time and power can exceed many weeks easily when increasing lattice parameters. To avoid this, we have to consider several options as mentioned in 5.

4. Results

In this section we will present the results of our investigation on the phase diagrams of $1+1$- and the $1+2$-dimensional version of the GN model in the (θ, μ)-plane. Both models will be studied first in translationally invariant calculation and examined in a precision test with continuum results. Then the inhomogeneous result and the form of spatially dependent condensates will be presented. First, we show the two-dimensional results used as a test on our numerical methods.

4.1. 1+1-dimensional Gross-Neveu model

In the two-dimensional version of the problem the full phase diagram has already been computed analytically in 2003 [Th03]. This solution we will use as a test for our numerical computation methods. The order parameter m in this diagram breaks the chiral symmetry dynamically and therefore, corresponds to our chiral condensate.

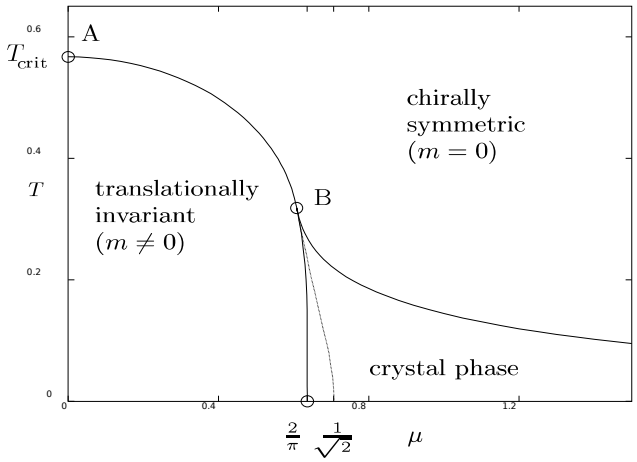

Figure 4.1: Phase diagram of the two-dimensional GN model, with the dashed line being the former solution for the homogeneous case [Th03]

From point A to B we have a second order boundary between the translationally invariant and the chirally symmetric phase. B is called tricritical point, because the three phases are at equilibrium at B. The dashed line is the old phase boundary from a earlier translationally invariant calculation of the phase diagram and symbolizes a first order boundary to the chirally symmetric phase. The crystal phase mentioned here is the spatially dependent phase found in 2003, in which the condensate's shape has a kink-antikink shape. The same solution with some finite size artifacts was also found by [dFW06].

4.1.1. Precision of mode calculation

First, we will investigate the precision of our mode computation in dependence on our lattice parameters. This is done by a comparison of the critical temperature θ_c of the phase boundary at vanishing chemical potential with the analytical value. In consequence, we can investigate the precision of our temperature calculation via comparison with the analytical value $\theta_{c,\text{ analytical}} = 5.66933 \cdot 10^{-1}\sigma_0$.

$N_{t,c}$	coupling constant λ	lattice distance $a_t[\sigma_0]$	θ_c $[10^{-1}\sigma_0]$	Percentage deviation from $\theta_{c,\text{ analytisch}}$
4	0.611	$7.15 \cdot 10^{-2}$	5.71997	0.893
6	0.526	$4.76 \cdot 10^{-2}$	5.70741	0.671
8	0.480	$3.56 \cdot 10^{-2}$	5.69623	0.474
10	0.449	$2.84 \cdot 10^{-2}$	5.68932	0.353
12	0.427	$2.37 \cdot 10^{-2}$	5.68484	0.274
16	0.396	$1.77 \cdot 10^{-2}$	5.67946	0.178
32	0.337	$8.90 \cdot 10^{-3}$	5.67260	0.058

Table 6: Precision of mode calculation for $1+1$-dimensional GN-model with spatial lattice extent $L = 480$

As a check, we do a linear approximation on the behavior of θ_c on dependence on the lattice spacing in time a_t. This approximation is used to calculate the expected value for $a_t = 0$, which is the limit to the continuum space-time, to compare with the analytical value of 4.1.

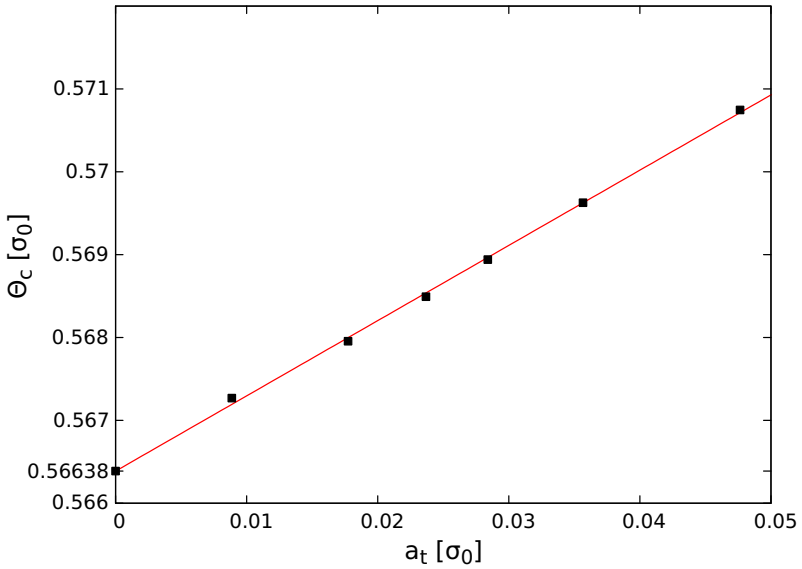

Figure 4.2: Continuum limit for critical temperatur at $\mu = 0$, the black points are the data from 6, the red line shows the linear fit to the data

With this limit we can evaluate whether our discretization of space-time has effected the physics of our theory. The constructed value from the linear approximation of data differs from the analytical solution within 0.09%.

4.1.2. Homogeneous phase diagram

In the translationally invariant case we can apply, compared to the inhomogeneous case, a big lattice size both in time and spatial direction, because we only have to minimize in one variable and use our analytical simplification as presented in 2.2.2 . This leads to a relatively small runtime (see 3.3.1).

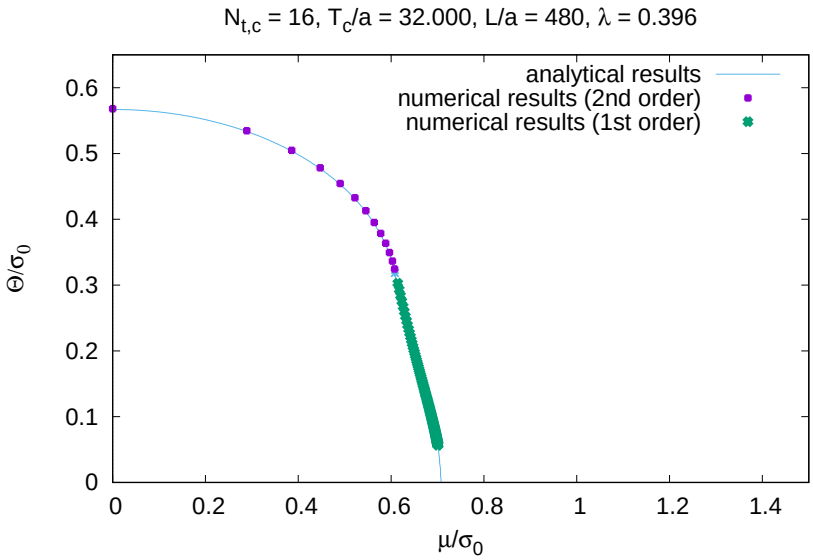

Figure 4.3: Phase diagram of the two-dimensional GN model, numerical results in comparison the homogeneous case from 4.1

As the blue line is the data extracted from the analytical solution, we see that the correct phase diagram is reproduced. We left out some data around the blue point that is the analytically found tricritical point to show that we also reproduced the exact same point. Above it was also explained why we cannot cover the phase boundary at $\theta = 0$, because the number of modes we have to include in our calculation goes asymptotically against infinity for $\theta \to 0$. Hence, measured by our expectation the test of our implemented functionalities for finding the homogeneous phase boundary was successful.

4.1.3. Inhomogeneous phase boundary

As the inhomogeneous phase diagram's computation time depends a lot on the lattice extent, we need to scale down the external parameter L and $N_{t,c}$, because already for smaller lattice sizes the calculation requires a lot more computation power and time (see 3.3.1). To ensure that the numerical errors do not emerge, the calculation have been conducted on the FUCHS-CSC high performance computers.

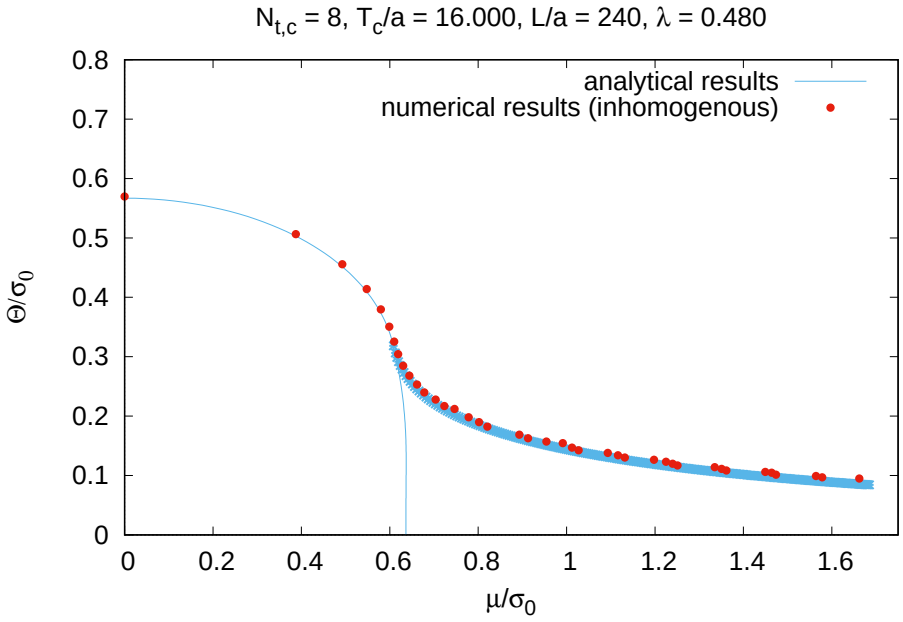

Figure 4.4: Inhomogeneous phase boundary of the two-dimensional GN model between chirally restored and inhomogeneous phase via instability analysis

Although the computation has been parallelized for each phase point, we find small incommensurability effects in regions of higher chemical potential, as described by [dFW06], from the finite spatial volume with the current setup resulting in small fluctuations in the boundary. Nevertheless, we can at least reproduce a phase limit nearby analytical solution. If we applied an even larger L, the rest of these incommensurability effects would vanish and we get a phase boundary identical with the analytical solution up to small errors in temperature calculation caused by our mode calculation with finite mode number. We also want to investigate the form of our chiral condensate in this region. Although we have not minimized the effective action, we can guess a direction which leads to a smaller action than the $\sigma = 0$ solution by the form of the eigenvectors corresponding to the negative eigenvalues.

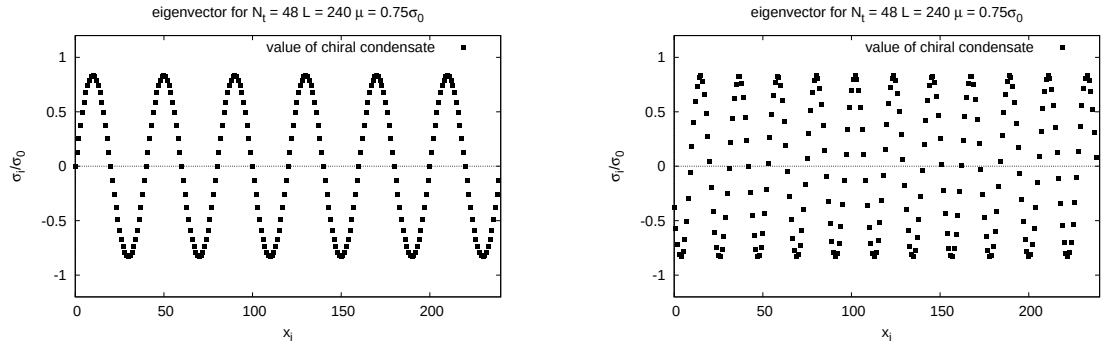

(a) $\mu = 0.75\sigma_0$ (b) $\mu = 1.2\sigma_0$

Figure 4.5: Eigenvector of Hessian matrix corresponding to negative eigenvalue

In different regions the eigenvectors have a wave form but the wavelength differs with the chemical potential. In figure 4.5 (a) we obtain a wavelength of $48a_t$, while for $\mu = 1.2\sigma_0$ we get a wavelength of $22a_t$. Since we obtain several eigenvectors at one point, we also get different wavelengths. But in general, our investigations reveal that the wavelength gets shorter when increasing the chemical potential.

We also check the form of eigenvectors in regions that cross the phase boundary of the inhomogeneous to the chirally broken phase. Here we obtain eigenvectors that contain the same value, but also vectors that behave like 4.5 with various wavelengths. As we can now use the eigenvectors as input for a computation of the action, we can compare the effective actions of both forms. At a certain chemical potential, the vectors with the same entries will have a lower action. This is no method to produce the missing boundary, as the eigenvectors only give a direction in the σ-vectorspace, that lowers the value of the effective action. They are not the solution of an exact minimization of the problem and therefore, are not suitable to compute the correct phase boundary. A true minimization is necessary to obtain the exact same phase boundary as [Th03]

4.2. 1+2-dimensional Gross-Neveu model

For the three-dimensional there also exists an analytical solution for the translationally invariant condensate from [Url03], that we can compare with our computation.

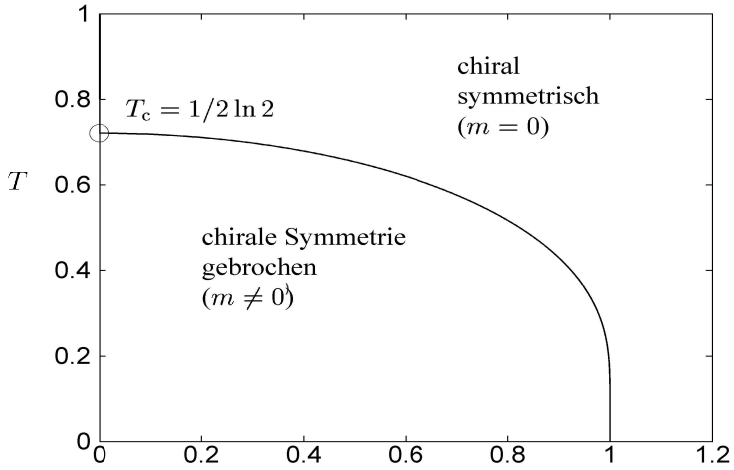

Figure 4.6: Phase diagram of the three-dimensional GN model for translationally invariant condensate in units of vacuum-fermion-mass (corresponds our σ_0) [Url03]

Because the original data from [Url03] is not available, we will compare our homogeneous solution via measurement in relation to the diagrams size to check our data with the diagram. As mentioned by [Url03, page 35], we find that the tricritical point, at which the order of boundary changes for finite chemical potential for two dimension, is located at $\mu = 0$. Consequently, the whole boundary is of first order besides the tricritical point, where we find a boundary of second order.

4.2.1. Precision of mode calculation

Again we investigate the precision of our mode calculation via the analytical solution of the critical temperature at $\mu = 0$ and a continuum limit. Therefore, we compare to [Url03]

$$\theta_{c,\text{ analytical}} = \frac{1}{2\ln(2)} \approx 0.721348\sigma_0.$$

Applying an adequate continuum limit for the data in table 7 is not possible, because it behaves not like a linear or quadratic function in the lattice distance. This is a result of several numerical errors, such as non-trivial cutoff effects, rounding error and other numerical errors, that have not been investigated yet. For sure, these errors have to

$N_{t,c}$	coupling constant λ	lattice distance a_t	θ_c $[10^{-1}\sigma_0]$	Percentage deviation from $\theta_{c,\text{ analytisch}}$
4	$1.02 \cdot 10^{0}$	$8.97 \cdot 10^{-2}$	7.17305	0.560
6	$9.85 \cdot 10^{-1}$	$6.06 \cdot 10^{-2}$	7.24820	0.481
8	$9.67 \cdot 10^{-1}$	$4.54 \cdot 10^{-2}$	7.26053	0.652
10	$9.57 \cdot 10^{-1}$	$3.63 \cdot 10^{-2}$	7.26006	0.646
12	$9.50 \cdot 10^{-1}$	$3.02 \cdot 10^{-2}$	7.25658	0.597
16	$9.42 \cdot 10^{-1}$	$2.27 \cdot 10^{-2}$	7.25033	0.511
24	$9.29 \cdot 10^{-1}$	$1.51 \cdot 10^{-2}$	7.23824	0.343

Table 7: Precision of mode calculation for $1+2$-dimensional GN-model with spatial lattice extent $L = 300$

be studied to ensure a more precise calculation. However, we see that for all setups in table 7 the calculation is within one percent of the analytical solution which should be sufficient for our purposes, since we want to explore the phase diagram at first.

4.2.2. Homogeneous phase diagram

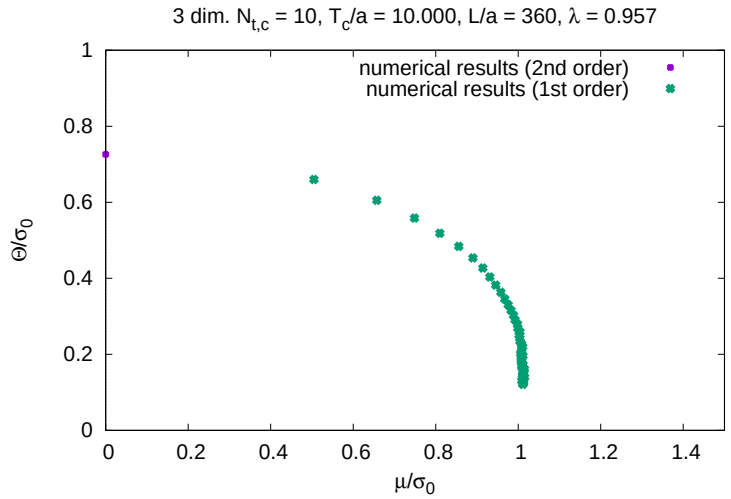

Figure 4.7: Phase diagram of the three-dimensional GN model for translationally invariant condensate, numerical result

By comparison with 4.6 we see the same phase diagram reproduced within numerical errors of around 1% in both chemical potential and temperature. This was tested by measuring the position of the boundary in relation to the size of both diagrams for several points resulting in a precision within one percent due to measuring errors. Notice that the

second order disappears completely except to the $\mu = 0$ point and a first order transition dominates the boundary. This is of interest, as in the two-dimensional case we see that the first order boundary disappears completely, when allowing spatial dependence for the condensate, and instead a boundary to the inhomogeneous phase comes up. With an instability analysis we can provide a first investigation of inhomogeneous phases in three dimensions.

4.2.3. Inhomogeneous phase boundary

For these computations we work with less precision in our bisection to save some computation time. The calculated value of the chemical potential, where the boundary occurs, is within a precision of $0.05\sigma_0$. Due to the enormous requirement of our code on computation power and time the diagram suffers from finite volume effects anyway, that result from small spatial and temporal extent. To justify that the discovery of instability for the chirally restored solution at large chemical potential is not just an artifact of our small lattice, we explored several lattice configuration. Nevertheless, the results should not be considered as exact phase diagrams, but as a first investigation of the region, where inhomogeneous phases occur. We confront the inhomogeneous result with the homogeneous ones for each setup to get a better idea of the form of the inhomogeneous phase in the $(\theta,\ \mu)$-plane. As we want to have a impression of the region, where inhomogeneous

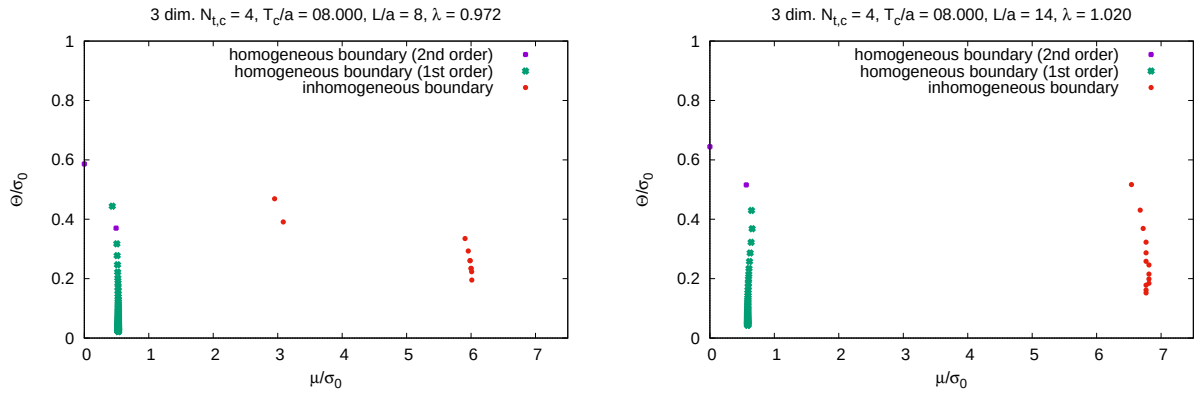

(a) 4×8 lattice

(b) 4×14 lattice

Figure 4.8: Inhomogeneous phase boundary of the three-dimensional GN model between chirally restored and inhomogeneous phase via instability analysis

phases occur, we also plot the homogeneous boundaries for the same lattice. Working on small lattice sizes also the homogeneous results suffer from finite volume effects that also cause a change in the order of the boundary at some points. For slightly larger spatial extent the instability analysis also yields a phase boundary in the same region as in 4.8. (b). Since we are only able to work on small volumes, it is an important task to ensure

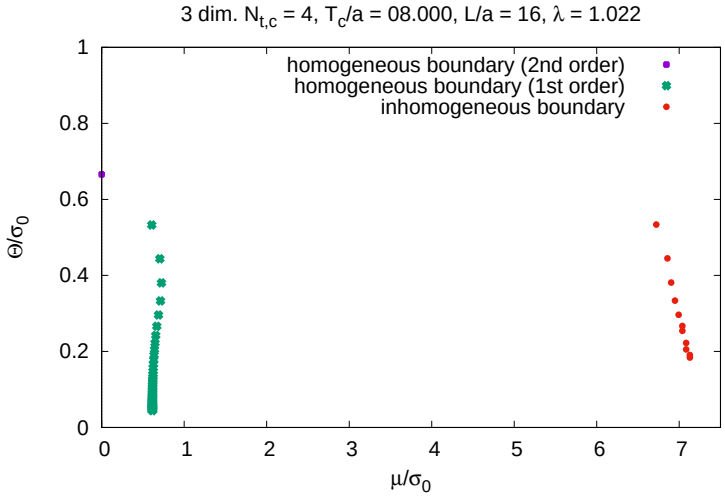

Figure 4.9: Inhomogeneous phase boundary of the three-dimensional GN model between chirally restored and inhomogeneous phase via instability analysis for 4×16 lattice

that the found inhomogeneous structures are no pure artifacts of lattice discretization and the small volume box. Thus, we look at the eigenvectors corresponding to negative eigenvalues. This is done on the 4×16 lattice. We find different types of configurations that lower the action compared to its value for vanishing σ. We examine the eigenvectors at both phase boundaries and in the middle of the region that we suspect be the inhomogeneous phase. We suspect some of the found eigenvectors to be lattice artifacts as they jump from their maximum value to their minimum between adjacent points. Here we present some eigenvectors we suspect to survive in a continuum calculation. The selection of this configurations is based on avoidance of modulations, in which the condensates value changes in a way that seems unlikely to be realized in a continuous space, and the knowledge of previous work [Url07, page 42], where a one-dimensional stripe ansatz has been found to have the same energy as the translationally invariant ansatz. This choice is also made out of intuition and should be confirmed with a real minimization algorithm in the future. Our figures visualize the value of the condensate in a map, where the color, that a point shows, corresponds to the value in units of σ_0. All configurations are plotted in the appendix A.1.
The figure 4.10 (a) shows a one dimensional modulation, that probably corresponds to the analytical stripe ansatz mentioned above. Also we find some two-dimensional modulations, where the condensate forms some sort of cupolas. For lower chemical potential the eigenvalues differ a bit. The stripe form appears in smaller wavelength 4.11 and some of the more complicated structures do not occur anymore. The cupola modulations disappears near the boundary to the broken phase.

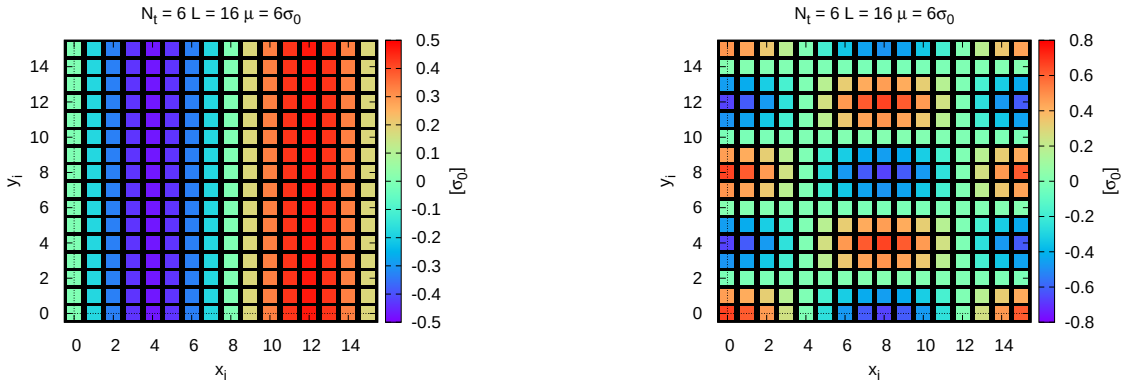

(a) stripe modulation

(b) cupola modulation

Figure 4.10: Candidates for the form of the chiral condensate in the inhomogeneous phase

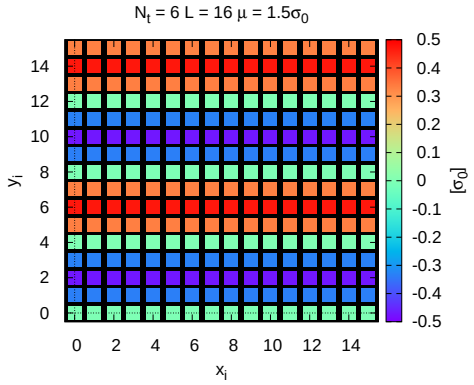

Figure 4.11: Stripe modulation, smaller μ

5. Conclusion and Outlook

We start to develop numerical methods for the investigation of phase diagrams on the two-dimensional Gross-Neveu model. The implemented phase boundary determination works well in the homogeneous case. The inhomogeneous phase is determined by an instability analysis of the chirally restored solution, since we are well aware of the homogeneous phase boundary and therefore, could perfectly identify the boundary between chirally restored and inhomogeneous phase. The other boundary to the chirally broken phase could not be calculated but one can guess its position out of the eigenvectors occurring in the instability analysis in this region. For the three-dimensional model we could reproduce the same phase diagram with translationally invariant condensate as in [Url03]. Allowing translationally asymmetric configurations for the chiral condensate we find indications of a new inhomogeneous phase. In this region spatially dependent configurations, for example one-dimensional and cupola shaped modulations, that are found by instability investigation, lead to lower actions than the vanishing condensate. These results suffer from finite volume effects, since calculations with larger lattice parameters exceed a computation time of many weeks.

First of all, it is important to confirm our inhomogeneous boundary results in the $1+2$-dimensional GN model with larger lattice extent. Hence, we have to reduce the order of dependence on the lattice size with better implementation methods to enable more realistic calculations. This could be done by restricting to the one-dimensional modulation of the condensate, although we would ignore several modulations depending on both spatial directions. It is very important to implement a minimization algorithm in the homogeneous phase. This would allow us to compute the real phase boundary and at the same time to study the physical configuration of the condensate in the inhomogeneous phase. After finding this configuration we would like to explore its behavior for variation of chemical potential and temperature within the phase.

When these investigations are finished, we would like to extend our studies of inhomogeneous phases to other models, for example in consideration of isospin or strangeness chemical potential. Another model of interest is the Nambu-Jona-Lasinio (NJL) model.

A. Appendix

A.1. Inhomogeneous eigenvectors of Hessian matrix for $1+2$ dimensions

In the three-dimensional GN model the instability analysis via Hessian matrix of the chirally restored solution delivers several possible directions that lower the action compared to the vanishing condensate. Some of these eigenvectors seem to be lattice artifacts, others could also survive in a continuum calculations. For completeness all types of found eigenvectors for $N_t = 6$ and $\mu = 1.5\sigma_0, 4\sigma_0, 6\sigma_0$ are presented here. Our figures visualize the value of the condensate in a map, where the color, that a point shows, corresponds to its value in units of σ_0.

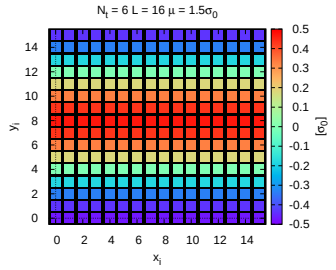

(a) stripe modulation, long wavelength

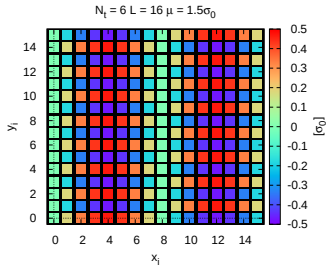

(b) waves in one direction, jumping from maximum to minimum value on the other direction

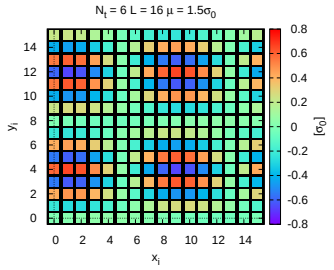

(c) huge absolute values are together, jumping from maximum to minimum value

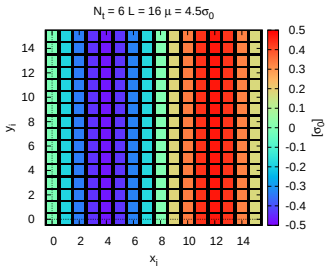

(d) stripe modulation

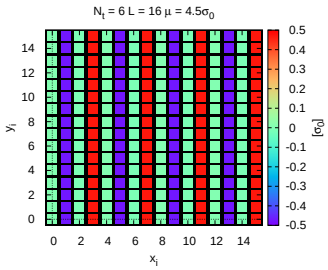

(e) probably a lattice artifact

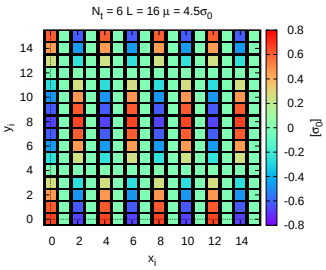

(f) waves shifted against each other

Figure A.1: Form of the chiral condensate in the inhomogeneous phase implied by the eigenvectors of the Hessian matrix, figures a, b, c for $\mu = 1.5\sigma_0$ & d, e, f for $\mu = 4.5\sigma_0$

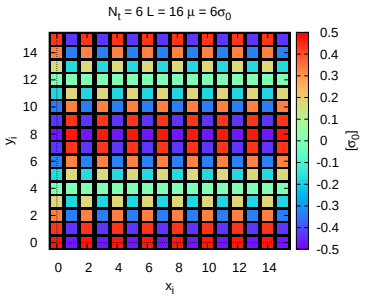

(a) waves in one direction, shifted against each other

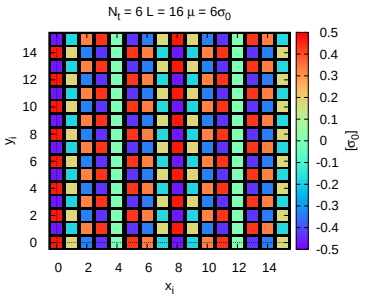

(b) complex structure, jumping from maximum to minimum value on neighbored points

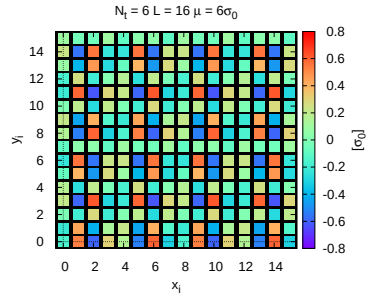

(c) complex structure

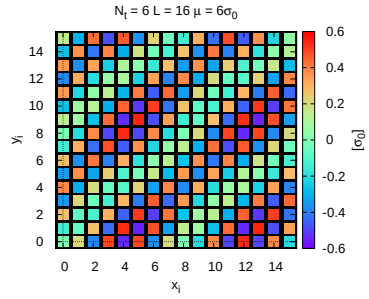

(d) sort of diagonally shifted waves huge value differences in neighbored points

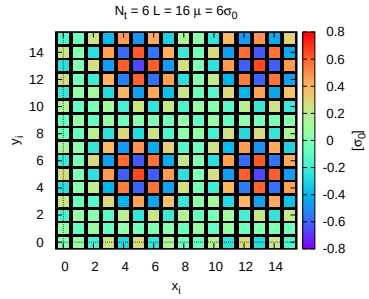

(e) points with huge absolute value collected together

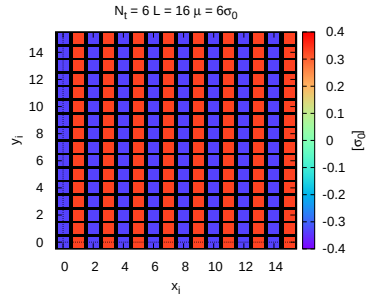

(f) jumping from maximum to minimum value, probably lattice artifact

Figure A.2: Form of the chiral condensate in the inhomogeneous phase implied by the eigenvectors of the Hessian matrix, $\mu = 6\sigma_0$

References

[Bub15] M. Buballa and S. Carignano, Prog. Part. Nucl. Phys. 81, 39 (2015) doi:10.1016/j.ppnp.2014.11.001 [arXiv:1406.1367 [hep-ph]].

[Th03] M. Thies and K. Urlichs, Phys. Rev. D 67, 125015 (2003) doi:10.1103/PhysRevD.67.125015 [hep-th/0302092].

[GN74] D. J. Gross and A. Neveu, Phys. Rev. D 10, 3235 (1974).

[Wag18] Marc Wagner, "Inhomogeneous phases at high density in QCD-inspired models", talk at Friedrich-Schiller-University Jena (15 May 2018) `https://th.physik.uni-frankfurt.de/~mwagner/talks/Jena_2018.pdf` (20th September 2018, 17:51)

[Wagup] Marc Wagner, unpublished notes

[Park05] Park, lecture notes, summer school Modave (2005) `http://www.ulb.ac.be/sciences/ptm/pmif/Rencontres/ModaveI/gamma.pdf` (19th August 2018, 22:07)

[Url03] Konrad Urlichs, "Das Phasendiagram des Gross-Neveu-Modells", Diploma thesis, Friedrich-Alexander-University, Erlangen-Nürnberg (2003)

[Url07] Konrad Urlichs, "Baryons and baryonic matter in four-fermion interaction models", Doctoral thesis, Friedrich-Alexander-University, Erlangen-Nürnberg (2007)

[Gm18] Wikipedia article, Higher-dimensional gamma matrices `https://en.wikipedia.org/wiki/Higher-dimensional_gamma_matrices` (20th August 2018, 17:35)

[GL10] C.Gattringer & C.B.Lang, Quantum Chromodynamics on the Lattice, Springer Verlag (2010)

[dFW06] P. de Forcrand and U. Wenger, PoS LAT 2006, 152 (2006) doi:10.22323/1.032.0152 [hep-lat/0610117].

Selbstständigkeitserklärung

Hiermit erkläre ich, dass ich die Arbeit selbstständig und ohne Benutzung anderer als der angegebenen Quellen und Hilfsmittel verfasst habe. Alle Stellen der Arbeit, die wörtlich oder sinngemäß aus Veröffentlichungen oder aus anderen fremden Texten entnommen wurden, sind von mir als solche kenntlich gemacht worden. Ferner erkläre ich, dass die Arbeit nicht - auch nicht auszugsweise - für eine andere Prüfung verwendet wurde.

Frankfurt, den 25.September 2018

_____

Marc Winstel